SCIENCE CHINA
Technological Sciences

• RESEARCH PAPER •

July 2026, Vol. 69, Iss. 7, 1720201:1–1720201:12
https://doi.org/10.1007/s11431-025-3277-2

Immuno-nanoinhibitor potentiates molecular targeted therapy of T-cell acute lymphoblastic leukemia

Chenming LI[1†], Zhenzhen ZHAI[1†], Lin CHEN[1], Li CAO[2], Huanli SUN[1*] & Zhiyuan ZHONG[1,2*]

[1] *State Key Laboratory of Bioinspired Interfacial Materials Science, Biomedical Polymers Laboratory, College of Chemistry, Chemical Engineering and Materials Science, Soochow University, Suzhou 215123, China*
[2] *College of Pharmaceutical Sciences, Soochow University, Suzhou 215123, China*

Received December 4, 2025; accepted March 2, 2026; published online June 17, 2026

Abstract T-cell acute lymphoblastic leukemia (T-ALL), with few targeted therapies in the clinic, is the most problematic blood cancer. Here, we report an immuno-nanoinhibitor (iNAHI) that selectively delivers volasertib, an inhibitor of polo-like kinase 1 (PLK1), to T-ALL cells for high-efficacy molecular targeted therapy. The iNAHI, with an average of 3.5 daratumumab antibodies per nanoparticle, possessed a high inhibitor-to-antibody ratio of ca. 600, enabling effective delivery of volasertib at a low antibody dosage. As a result, iNAHI significantly boosts PLK1 downregulation, cell cycle blockade and apoptosis in CD38-positive T-ALL cells compared with free volasertib and nontargeted nanoinhibitor. Therapeutic studies in mice with orthotopic CCRF-CEM T-ALL revealed potent suppression of leukemia burden and extramedullary invasion at a low iNAHI dose of 9 mg volasertib equiv./kg, leading to significant survival benefits with negligible adverse effects. This immuno-nanoinhibitor provides a promising targeted treatment strategy for T-ALL.

Keywords acute leukemia, nanomedicines, molecular targeted drug, targeted therapy, antibody-drug conjugates

Citation: Li C M, Zhai Z Z, Chen L, et al. Immuno-nanoinhibitor potentiates molecular targeted therapy of T-cell acute lymphoblastic leukemia. Sci China Tech Sci, 2026, 69(7): 1720201, https://doi.org/10.1007/s11431-025-3277-2

1 Introduction

T-cell acute lymphoblastic leukemia (T-ALL) is the most problematic blood cancer originating from the malignant expansion of T-cell progenitors [1–3]. Patients, regardless of genotype, are routinely treated with multidrug intensive chemotherapy [4–6]. However, relapse or drug resistance frequently occurs, and affected patients often face a dismal prognosis, as effective salvage therapies remain scarce, and durable remission is rarely achieved [7–9]. The nucleoside analog nelarabine stands as the lone approved drug for relapsed/refractory T-ALL but provides only modest benefit and has severe neurotoxicity [10,11].

Advances in T-ALL biology have promoted preclinical and clinical testing of small molecular targeted agents and antigen-directed therapies, yet none have secured regulatory approval [12,13]. For example, although antibody-based therapeutics and chimeric antigen receptor (CAR)-T cells have revolutionized the therapeutic landscape for multiple cancers [14–18], they remain in the early clinical stage of T-ALL. The major obstacle lies in the overlap of T-ALL surface antigens with those of normal T cells. CD7-targeted CAR-T cells, the most extensively investigated targeted therapy in T-ALL trials, are generally perplexed with fratricide and the risk of leukemic cell contamination as a result of the overlap of the CD7 antigen [19,20]. CD38, a clinically validated target in multiple myeloma, is uniformly expressed in T-ALL patients [21–23]. Leveraging the approved anti-CD38 antibody daratumumab in combination with chemotherapy has improved the response rate in relapsed/refractory T-ALL patients [24–26]. However, naked daratumumab requires high-dose administration, which may

† These authors contributed equally to this work.
* Corresponding author (email: sunhuanli@suda.edu.cn; zyzhong@suda.edu.cn)

© Science China Press 2026

enhance on-target off-tumor toxicity against CD38-expressing normal lymphocytes [27,28]. Moreover, its combination with chemotherapeutics inevitably causes severe damage to healthy tissues and the immune system.

In this study, we engineered a CD38-targeting immuno-nanoinhibitor (iNAHI) by arming the polo-like kinase 1 (PLK1) nanoinhibitor polymersomal volasertib with daratumumab for high-efficacy molecular targeted therapy of T-ALL (Figure 1(a)). PLK1 is a validated oncogene that is upregulated in a broad spectrum of cancers, including T-ALL, and its selective inhibitor volasertib has shown clinical efficacy in both leukemia and solid tumors [29–31]. iNAHI with a high inhibitor-to-antibody ratio of ca. 600 enables the selective and effective delivery of volasertib to CD38-positive T-ALL cells at a relatively low daratumumab dosage, thereby minimizing potential off-tumor toxicity to normal cells. Consequently, iNAHI enhanced PLK1 inhibition and anti-T-ALL efficacy compared with free volasertib and nontargeted nanoinhibitor (NAHI). Moreover, iNAHI with enhanced bone marrow accumulation potently suppressed leukemia expansion and extramedullary infiltration in orthotopic CCRF-CEM T-ALL-bearing mice, leading to significantly improved survival benefits with negligible adverse effects.

2 Experimental section

2.1 Materials

Daratumumab (Xi'an Janssen Pharmaceutical Co., Ltd.), volasertib (99.4%, Med Chem Express), *N*-hydroxysuccinimidyl ester-tetra(ethylene glycol)-dibenzocyclooctyne (NHS-PEG_4-DBCO, Cat: 1427004-19-0, 98%, BroadPharm®), allophycocyanin (APC) anti-human CD38 (APC-ahuCD38,

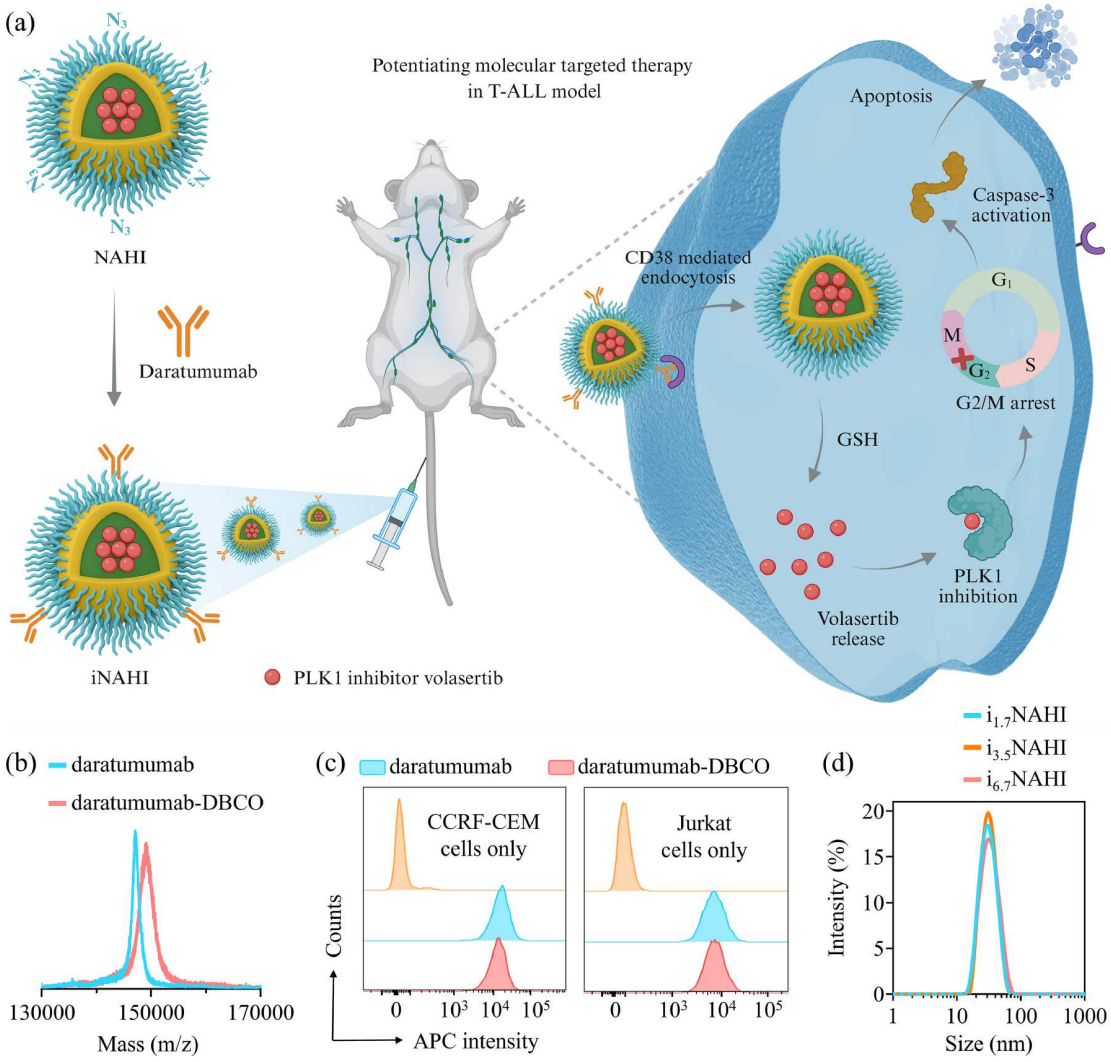

Figure 1 (a) Schematic illustrating the fabrication of CD38-targeted immuno-nanoinhibitors (iNAHI) for molecular targeted therapy in an orthotopic T-ALL mouse model. (b) Matrix-assisted laser desorption-ionization time-of-flight mass spectrometry (MALDI-TOF-MS) spectra of daratumumab and daratumumab-DBCO. (c) Affinity of daratumumab-DBCO for CD38-overexpressing CCRF-CEM and Jurkat T-ALL cells. (d) Size distributions of iNAHIs with different daratumumab densities.

Cat: 303510, Biolegend), APC anti-human IgG Fc (APC-ahuFc, Cat: 410711, Biolegend), APC anti-human CD45 (APC-ahuCD45, Cat: 304012, Biolegend), wheat germ agglutinin-AF488 (WGA-AF488, Thermo Fisher Scientific), 4′,6-diamidino-2′-phenylindole (DAPI, Beyotime Biotechnology), cyanine 5-NH_2 (Cy5, Beijing Fanbo Biochemicals Co., Ltd.), cell counting kit-8 (CCK-8, Suzhou Fcmacs Biotech Co., Ltd.), and Annexin V-APC/7-AAD apoptosis kit (MultiSciences) were ordered and used directly. Ultrafiltration tubes were purchased from Merck Millipore (MWCO: 10 kDa) and Sartorius (MWCO: 300 kDa). Poly (ethylene glycol)-*b*-poly(trimethylene carbonate-*co*-dithiolane trimethylene carbonate)-*b*-poly(aspartic acid) (PEG-P (TMC-DTC)-KD_{10}, 5.0-(15.0-2.0)-1.3 kg/mol) and N_3-PEG-P(TMC-DTC) (7.9-(15.1-2.0) kg/mol) copolymers were obtained following a synthetic protocol similar to that described in our earlier work [32,33].

2.2 Fabrication of immuno-nanoinhibitors (iNAHI)

Immuno-nanoinhibitors (iNAHI) were prepared via strain-promoted azide-alkyne cycloaddition, whereby the daratumumab antibody was clicked onto preformed azide-functionalized polymersomal volasertib nanoinhibitor (NAHI). NAHI was obtained from the coassembly of PEG-P (TMC-DTC)-KD_{10} with 2 wt% N_3-PEG-P(TMC-DTC) concurrent with volasertib encapsulation. The theoretical drug loading content of volasertib, denoting the mass of volasertib relative to the total mass of polymer and volasertib, was set at 16.7 wt%. The concentration of volasertib was determined via high-performance liquid chromatography (HPLC) with a mobile phase consisting of acetonitrile and water (0.15% triethylamine, adjusted to pH 7.0 with phosphoric acid) at a volumetric ratio of 60:40 (v/v), and detection was performed at a wavelength of 330 nm with the column temperature maintained at 35°C. The blank polymersomes (NA) were prepared similarly, and their molecular weight (MW) was determined by multi-angle laser light scattering coupled with gel permeation chromatography (MALS-GPC, Waters 1515-Wyatt DAWN HELEOS II).

To enable the click reaction, the CD38-targeted daratumumab antibody was first tagged with NHS-PEG_4-DBCO, similar to our previous reports [34,35]. Briefly, 100 μL of daratumumab solution (20 mg/mL) was diluted 1:1 with 100 μL of phosphate buffer (PB, 10 mmol/L, pH 8.5), after which 2.6 μL of NHS-PEG_4-DBCO solution (10 mg/mL in dimethyl sulfoxide) was added for 12 h of reaction at 25°C and 120 r/min. The reaction mixture was subsequently diluted with 2 mL of PBS and subjected to two cycles of centrifugal ultrafiltration (MWCO: 10 kDa) at 4°C (3000 r/min) to obtain daratumumab-DBCO. The concentration of daratumumab-DBCO was determined via a Waters 1515 HPLC system equipped with a size-exclusion chromatography column at a wavelength of 214 nm. The mobile phase consisted of phosphate-buffered saline (pH 6.8, PB: 50 mmol/L, NaCl 150 or 300 mmol/L) and acetonitrile at a volumetric ratio of 90:10 (v/v). The DBCO functionality of daratumumab-DBCO was measured by MALDI-TOF-MS (Bruker), using unmodified daratumumab as the benchmark. iNAHI with varying antibody densities was synthesized by modulating the molar feeding ratios of daratumumab-DBCO to the surface N_3 of NAHI to 0.25:1, 0.5:1, and 1:1. In brief, 50 μL of NAHI (20 mg/mL) was reacted overnight with 6.6, 13.1, or 26.2 μL of daratumumab-DBCO solution (4.6 mg/mL) under continuous shaking (120 r/min) at 25°C. The sample was subsequently diluted in 4-(2-hydroxyethyl)-1-piperazine ethanesulfonic acid (HEPES, 5 mmol/L, pH 7.4) and ultracentrifuged (58000 r/min, 4°C) to remove unconjugated daratumumab-DBCO, affording iNAHI. The concentrations of unconjugated daratumumab-DBCO in the supernatant were measured via HPLC, thus calculating the conjugation efficiency. The surface antibody density of the iNAHI was calculated based on the following equation:

$$\text{Number of daratumumab per iNAHI} = \frac{\text{Mass of conjugated daratumumab}}{\text{MW of daratumumab}} \times \frac{\text{MW of NA}}{\text{Mass of NA}}. \quad (1)$$

Cy5-labeled blank immuno-nanoformulations (iNA-Cy5) were engineered by clicking daratumumab-DBCO onto Cy5-labeled azide-functionalized polymersomes (NA-Cy5), which were obtained via the incorporation of 20 wt% PEG-P (TMC-DTC)-Cy5 during the assembly process.

2.3 CD38-targetability and cellular uptake studies

CD38 membrane expression in CCRF-CEM and Jurkat T-ALL cell lines was first analyzed by flow cytometry with APC-ahuCD38 staining. Briefly, 1×10^6 cells in 100 μL of PBS were stained with 5 μL of APC-ahuCD38 on ice for 30 min in darkness. Then, the stained cells were centrifuged, rinsed two times with PBS and resuspended in 500 μL of PBS for flow cytometry analysis. Unstained cells were used as a negative control.

The binding affinities of daratumumab and daratumumab-DBCO to CCRF-CEM and Jurkat cells were assessed through flow cytometry. Briefly, cells (1×10^6) were incubated with daratumumab or daratumumab-DBCO (1 μmol/L) on ice for 60 min, followed by staining with 5 μL of APC-ahuFc and flow cytometric analysis. The cells that were not incubated with the secondary antibody served as negative controls.

The T-ALL targetability of iNAHI at different targeting densities was studied in CCRF-CEM and Jurkat T-ALL cell lines using Cy5-labeled blank nanoformulations (iNA-Cy5), with nontargeted NA-Cy5 and human T cells of healthy origin serving as controls. First, the cellular uptake of

iNA-Cy5 was quantitatively analyzed via flow cytometry. Cells plated in 12-well plates (1.8 mL, 2×10^5 cells/well) were treated with 200 μL of iNA-Cy5 or NA-Cy5 (Cy5: 40 nmol/L) for 4 h under standard culture conditions. Afterwards, the cells were pelleted by centrifugation, rinsed twice with PBS, and resuspended in 400 μL of PBS for flow cytometric analysis.

On the basis of the flow cytometric results, we further visualized the cellular uptake of iNA-Cy5 at the optimized targeting density in CCRF-CEM or human T cells via confocal laser scanning microscopy (CLSM). The cells (0.8 mL, 5×10^5 cells/well) were seeded onto poly-*L*-lysine precoated cell slides in 24-well plates and cultured overnight to facilitate cell adhesion. Two hundred microliters of iNA-Cy5 or NA-Cy5 (Cy5: 1.6 μmol/L) was subsequently added for 4 h of incubation, and the cells were then rinsed three times with PBS. After fixation with 4% paraformaldehyde, the cells were incubated in the dark with WGA-AF488 (5 μg/mL) to stain the cell membranes and with DAPI (5 μg/mL) to counterstain the nuclei. Each staining step was interspersed with three gentle PBS washes. Finally, the slides were mounted with glycerol to capture images via CLSM.

2.4 Inhibitory effects of immuno-nanoinhibitors on T-ALL cells

The inhibitory effects of iNAHI on CCRF-CEM and Jurkat cells were evaluated via the CCK-8 assay, with normal human T cells serving as a control. Briefly, cells were seeded into 96-well plates (2×10^4 cells/well, $n = 6$), followed by the addition of 20 μL of iNAHI at varying antibody densities or control NAHI. The volasertib concentration in each well was 0.2–200 ng/mL for CCRF-CEM cells and 0.1–1000 ng/mL for Jurkat cells. Following 48 h of incubation, CCK-8 solution (10 μL) was added to each well and incubated for 4 h. The optical density of each well at 450 nm was determined via a microplate reader to calculate the cell viability by comparing experimental groups with control cells incubated with PBS. The cytotoxicity of iNAHI toward normal human T cells and that of blank iNA toward CCRF-CEM cells were assessed via a similar procedure.

2.5 Cellular protein regulation mediated by iNAHI

The levels of cellular PLK1 and cleaved caspase-3 in T-ALL cells pre- and post-treatment with CD38-targeted iNAHI were quantified by flow cytometry. Specifically, CCRF-CEM cells in 6-well plates (5×10^5 cells/well, $n = 3$) were incubated with 200 μL of PBS, free volasertib, NAHI, or optimized iNAHI (volasertib: 20 ng/mL) for 24 h. The cells were then harvested via centrifugation, rinsed two times with PBS, and resuspended in 800 μL of fixation/permeabilization concentrate. After incubation at room temperature for 40 min, the samples were further centrifuged and washed with PBS. Next, 100 μL of PLK1 antibody (HA500281, HUABIO) or cleaved caspase-3 antibody (9664T, Cell Signaling Technology) was added for 40 min of incubation, followed by washing with PBS. The cells were then stained with an AF 647-labeled goat anti-rabbit antibody (A21244, Invitrogen) on ice for 30 min. After two additional PBS washes, the cells were analyzed via flow cytometry.

2.6 Cell cycle arrest and apoptosis analysis

iNAHI-induced cell cycle blockade in CCRF-CEM cells was evaluated via propidium iodide (PI) staining and flow cytometry. Specifically, cells plated in 6-well plates (5×10^5 cells/well, $n = 3$) were cultured with free volasertib, NAHI, or iNAHI at 10 ng/mL volasertib, with PBS serving as a control. After overnight incubation, the cells were pelleted via centrifugation, rinsed two times with ice-cold PBS and resuspended in 1 mL of PBS. The cell suspension was slowly dripped into cold ethanol (4 mL) under vortex for overnight fixation at 4°C. Following two PBS washes, the cells were dispersed in 400 μL of PI solution, incubated at 37°C in darkness for 30 min, and then subjected to flow cytometric analysis.

The ability of iNAHI to induce apoptosis in CCRF-CEM cells was analyzed using an Annexin V-APC/7-AAD double-staining kit. The cells were plated in 6-well plates (5×10^5 cells/well, $n = 3$) and incubated with free volasertib, NAHI, or iNAHI at 20 ng/mL volasertib for 24 h. Afterwards, the cells were rinsed twice with PBS, resuspended in binding buffer and sequentially stained with Annexin V-APC (5 μL) and 7-AAD (10 μL) for immediate flow cytometry analysis. The cells incubated with PBS served as a control. To prepare positive controls for early and late apoptosis, one aliquot of PBS-treated cells was incubated in 500 μL of positive control solution at room temperature for 30 min and then mixed with an equal aliquot of PBS-treated cells resuspended in 500 μL of binding buffer. After rinsing with PBS, the cells were split into two tubes and stained with Annexin V-APC and 7-AAD, respectively, for analysis.

2.7 Biodistribution study in an orthotopic CCRF-CEM T-ALL mouse model

All animal experiments and operations were approved by the Soochow University Laboratory Animal Center and the Animal Care and Use Committee of Soochow University (approval No. SYXK 2021–0065). The *in vivo* targetability and biodistribution of the nanoinhibitor were monitored via Cy5-labeled formulations (iNA-Cy5 and NA-Cy5) via *in vivo* imaging system (IVIS). To establish the orthotopic T-ALL mouse model, CCRF-CEM cells (5×10^5 cells per mouse) were injected into the tail vein of B-NDG female mice (7–8 weeks old, Biocytogen Jiangsu Gene Bio-

technology Co., Ltd.), and the day served as the starting point, day 0. On day 24 postinoculation, the mice were randomly grouped and received a tail-vein injection of iNA-Cy5 or NA-Cy5 (200 μL, 0.05 μg Cy5 per mouse). At 1, 2, 4, and 8 h postinjection, whole-body Cy5 fluorescence images were acquired with IVIS. Following imaging at 8 h, the mice were euthanized, and their limbs were excised for capturing *ex vivo* fluorescence images.

2.8 *In vivo* anti-T-ALL activity of iNAHI

An orthotopic CCRF-CEM T-ALL mouse model was employed to investigate the *in vivo* anti-T-ALL activity of CD38-targeted iNAHI. Treatment was initiated on day 5 postinoculation via tail vein injection of iNAHI, NAHI (volasertib: 9 mg/kg) or PBS for five doses with a 4-day interval each. Each group consisted of eight mice, five of which were used for monitoring survival and body weight changes, and the remaining three mice were used for routine blood tests, leukemia infiltration, and histological analysis. Leukemia infiltration in the blood was monitored on days 27 and 36. Mouse body weight was recorded every two days, and survival and status were continuously monitored. On day 34 postinoculation, when the mice in the NAHI group were nearing the experimental endpoint, three mice in the iNAHI and NAHI groups designated for monitoring leukemia infiltration were sacrificed. Blood, liver, spleen, lungs, and hindlimbs were sampled for routine blood and leukemia burden analysis. T-ALL cells in single-cell suspensions derived from different samples were labeled with an APC-ahuCD45 antibody, and leukemia infiltration was analyzed by flow cytometry. Three mice in the PBS group were sacrificed at their experimental endpoint (day 27) for relevant analyses and served as controls. Additionally, major organs and hindlimbs from the mice in all the groups were collected, fixed in 4% paraformaldehyde, embedded in paraffin, stained with hematoxylin and eosin (H&E), and subjected to pathological and histological evaluations.

2.9 Statistical analysis

Data are shown as the mean ± standard deviation (SD) and were processed in GraphPad Prism 8. Group differences were compared by one-way analysis of variance (ANOVA) with Tukey's post hoc test or by Student's *t* test where appropriate. Kaplan–Meier survival curves were constructed and compared via the log-rank test. $*p < 0.05$, $**p < 0.01$, $***p < 0.001$, and $****p < 0.0001$.

3 Results and discussion

3.1 Fabrication and characterization of immuno-nanoinhibitors (iNAHI)

The lack of safe and effective targeted therapeutics has severely compromised the prognosis of T-ALL patients. CD38, a clinically validated target for multiple myeloma patients [27], was leveraged herein for targeted delivery of the PLK1 inhibitor volasertib to potentiate molecular targeted therapy of T-ALL. Post-clicking the daratumumab antibody onto the surface of a polymersomal volasertib-based nanoinhibitor (NAHI), which was obtained via the assembly of PEG-P(TMC-DTC)-KD_{10} with 2 wt% N_3-PEG-P(TMC-DTC) concurrent with electrostatic interaction-driven volasertib encapsulation (Figure S1(a)), afforded CD38-targeted iNAHI. The NAHI containing 13 wt% volasertib had a particle size of approximately 28 nm and a low polydispersity index (PDI) of 0.08 (Figure S1(b) and Table 1). Blank NA exhibited a number-average molecular weight of 7.881×10^6 g/mol, corresponding to an aggregation number of 338 (Figure S2). To enable surface clicking, daratumumab was first conjugated with NHS-PEG_4-DBCO via an amidation reaction, yielding daratumumab-DBCO with 2.8 DBCO moieties per antibody on average (Figure 1(b)). Importantly, DBCO functionalization did not affect the affinity of daratumumab for CCRF-CEM or Jurkat cells (Figure 1(c)), which endogenously overexpress CD38 (Figure S3). The click reaction of daratumumab-DBCO with azide on the surface of NAHI was nearly quantitative at molar ratios of 0.25:1, 0.5:1, and 1:1, resulting in $i_{1.7}$NAHI, $i_{3.5}$NAHI, and $i_{6.7}$NAHI with 1.7, 3.5 and 6.7 daratumumab antibodies on each NAHI, respectively (Table 1). The resulting iNAHI featured a high inhibitor-to-antibody ratio (313–1235) and exhibited a small particle size of approximately 30 nm and a relatively low PDI of 0.06–0.10 (Figure 1(d) and Table 1).

Table 1 Characterization of the iNAHI with different daratumumab antibody densities

Nanoinhibitor	Molar ratio of antibody to N_3	Conjugated daratumumab [a]		Inhibitor-to-antibody ratio	Size (nm) [b]	PDI [b]
		Efficiency (%)	No. per NAHI			
NAHI	/	/	/		28.3 ± 0.3	0.08 ± 0.01
$i_{1.7}$NAHI	0.25:1	100	1.7	1235	29.8 ± 0.2	0.06 ± 0.03
$i_{3.5}$NAHI	0.5:1	100	3.5	600	30.8 ± 0.2	0.10 ± 0.02
$i_{6.7}$NAHI	1:1	98.5	6.7	313	30.6 ± 0.4	0.07 ± 0.03

a) Determined by HPLC; b) measured by dynamic light scattering (DLS).

3.2 *In vitro* selectivity and anti-T-ALL effect of iNAHI

CD38 is markedly overexpressed in T-ALL patients, with 97.9% of newly diagnosed patients exhibiting high surface levels and no significant change in matched relapsed samples [36]. This has sparked intense interest in targeting CD38 for T-ALL therapy. CCRE-CEM and Jurkat cells with elevated CD38 expression were employed to investigate the targetability and anti-T-ALL effect of iNAHI. To evaluate the targeted cellular uptake of iNAHI, Cy5-labeled nanoformulations, including iNA-Cy5 with different daratumumab densities and nontargeted NA-Cy5, were employed. As shown in Figure 2(a), engineering iNA-Cy5 with 1.7, 3.5 or 6.7 daratumumab ligands significantly increased uptake in CCRF-CEM cells by 3.6–5.9-fold compared with that of NA-Cy5, with the uptake nearly plateauing at a daratumumab density of 3.5. A similar uptake trend was further corroborated in Jurkat cells (Figure 2(b)). Importantly, the association of $i_{3.5}$NA-Cy5, hereinafter termed iNA-Cy5, with normal human T cells paralleled that of NA-Cy5 (Figure 2(c)) and was 15–24-fold lower than that of CCRF-CEM T-ALL cells. CLSM images further revealed that CCRF-CEM cells treated with iNA-Cy5 presented markedly higher intracellular Cy5 fluorescence than those treated with nontargeted NA-Cy5 and T cells incubated with iNA-Cy5 (Figure 2(d) and (e)).

Consistent with the cellular uptake data, iNAHI, regardless of daratumumab density, markedly outperformed nontargeted NAHI in inhibiting the proliferation of CCRF-CEM cells, with $i_{3.5}$NAHI conferring the strongest anti-T-ALL potency (Figure 2(f)). Specifically, $i_{3.5}$NAHI presented an half maximal inhibitory concentration (IC_{50}) value of

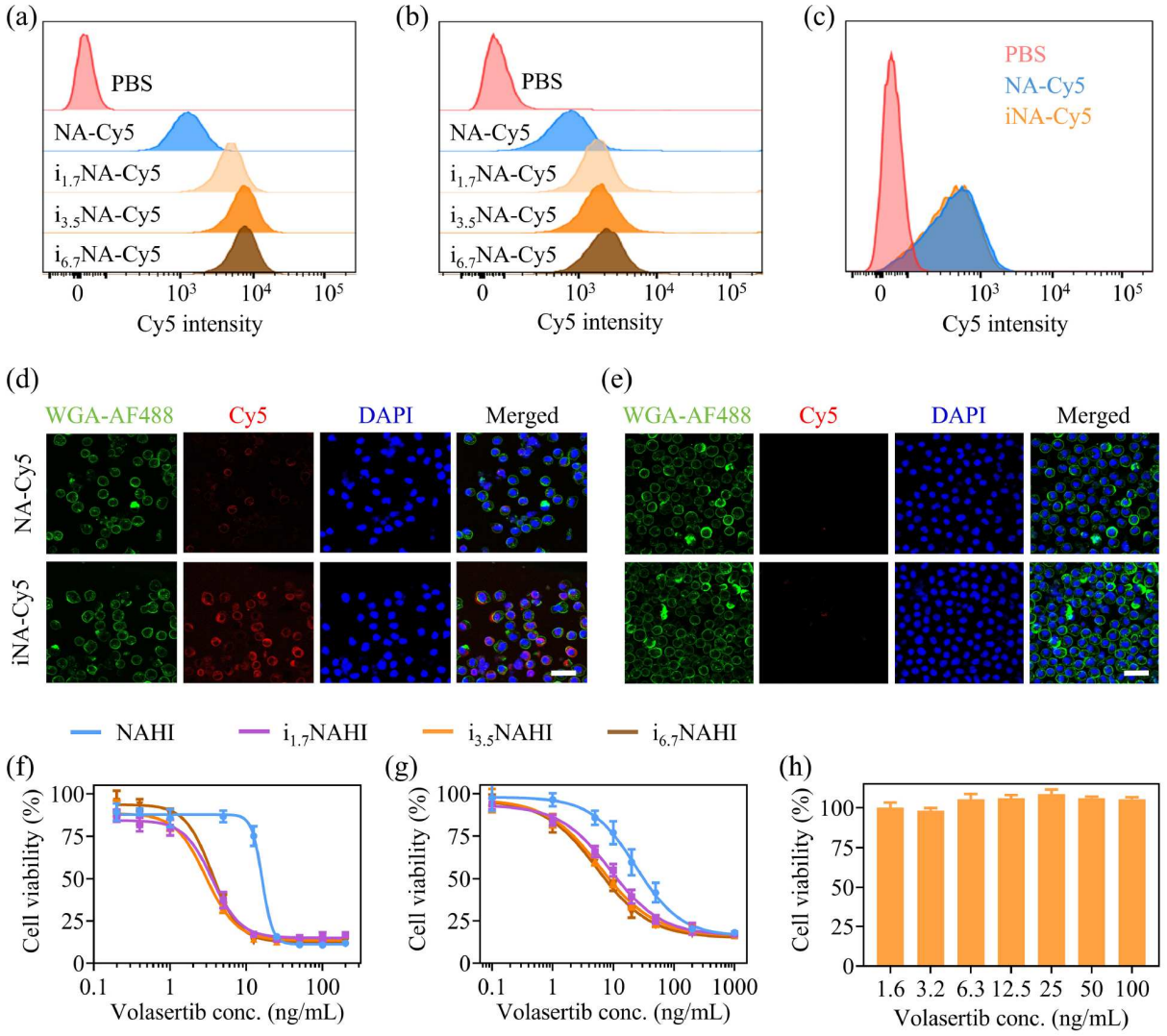

Figure 2 Cellular uptake and anti-T-ALL studies. Flow cytometric analysis of (a) CCRF-CEM cells and (b) Jurkat cells after 4 h of incubation with iNA-Cy5 at various daratumumab densities. (c) Association of $i_{3.5}$NA-Cy5 and NA-Cy5 with human T cells. CLSM snapshots of (d) CCRF-CEM and (e) human T cells after 4 h of exposure to iNA-Cy5 or NA-Cy5 (scale bars: 25 μm). Anti-T-ALL activity of iNAHI with varying daratumumab densities in (f) CCRF-CEM cells and (g) Jurkat cells, with nontargeted NAHI used as a control (n = 6). (h) Cytotoxicity of $i_{3.5}$NAHI against human T cells (n = 6).

3.0 ng/mL, which was 5.4-fold lower than that of NAHI (IC_{50}: 16.3 ng/mL). Similarly, iNAHI also displayed 3.7-fold higher anti-T-ALL activity than NAHI in Jurkat cells (IC_{50}: 8.5 vs. 31.6 ng/mL) (Figure 2(g)). Notably, iNAHI showed no appreciable toxicity toward normal human T cells, with viability remaining above 95% even at elevated volasertib concentrations up to 100 ng/mL (Figure 2(h)), underscoring its ability to selectively inhibit T-ALL cells. Moreover, blank iNA, regardless of daratumumab densities, was nontoxic to CCRF-CEM cells at NA concentrations of 5–500 μg/mL (Figure S4). In subsequent studies, iNAHI with 3.5 daratumumab molecules on the surface was employed, hereafter referred to simply as iNAHI.

The PLK1 inhibitor volasertib is known to selectively block PLK1 kinase activity and provoke cell cycle arrest and apoptosis in cancer cells [37,38]. Therefore, the cell cycle distribution and apoptosis of CCRF-CEM cells, as well as the levels of intracellular proteins, such as PLK1 and cleaved caspase-3, after different treatments were evaluated via flow cytometry. As shown in Figure 3(a), iNAHI treatment effectively downregulated the PLK1 protein level in CCRF-CEM cells, and the fraction of PLK1-positive cells decreased sharply from 81.8% in PBS-treated controls to 16.5%, which was significantly lower than that in the free volasertib and NAHI control groups (76.0%). Downregulation of the PLK1 protein by volasertib and other PLK1 inhibitors has been observed in various solid tumor cells [39–41]. The underlying mechanism is likely that kinase inhibition activates the ubiquitin ligase APC/C, thereby routing PLK1 for proteasomal degradation [42]. Consistently, iNAHI treatment markedly increased the G2/M fraction from 5.6% in the PBS-treated control group to 44.4%, surpassing the level achieved with free volasertib (9.5%) or nontargeted NAHI (24.5%) (Figure 3(b)). Apoptosis analysis further revealed

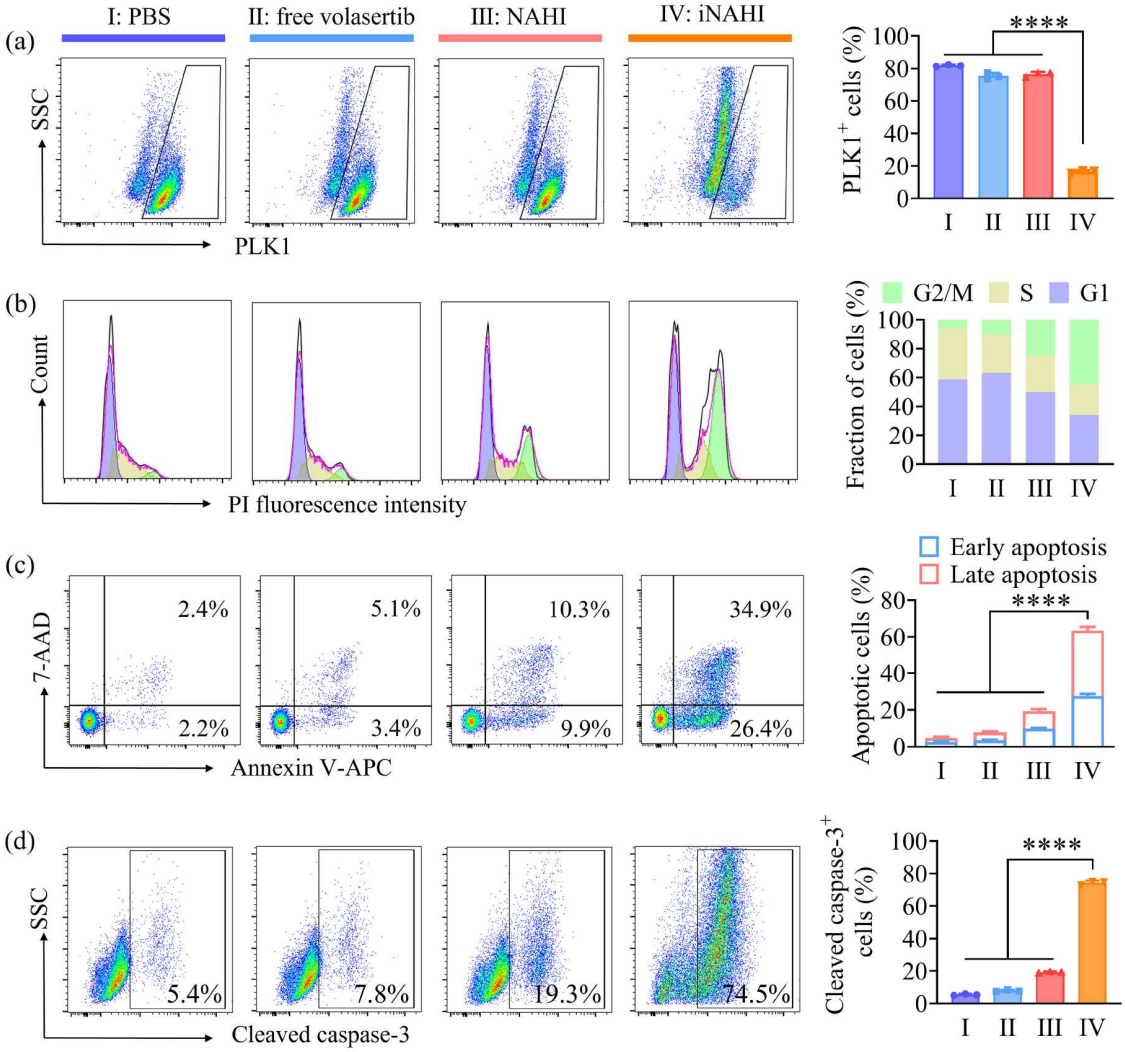

Figure 3 Protein regulation, cell cycle distribution and apoptosis profiles of CCRF-CEM cells after different treatments, including PBS, free volasertib, NAHI and iNAHI. Flow cytometric analysis of (a) PLK1 protein expression, (b) cell cycle distribution, (c) apoptosis, and (d) cleaved caspase-3 protein expression (n = 3). ****p < 0.0001.

that iNAHI triggered the highest level of apoptosis in CCRF-CEM cell lines, with 61.3% of the population displaying apoptotic markers, which was 7.2- and 3.0-fold greater than that in the free volasertib (8.5%) and NAHI (20.2%) groups, respectively (Figure 3(c)). To corroborate the elevated apoptosis rate, we next assessed the levels of cleaved caspase-3 protein as a biochemical readout of intrinsic apoptosis [43,44]. Following iNAHI treatment, the percentage of cleaved caspase-3-positive cells sharply increased to 74.5%, which was significantly greater than that following free volasertib (7.8%) or NAHI treatment (19.3%) (Figure 3(d)). Collectively, these findings demonstrate that iNAHI can selectively target T-ALL cells, downregulate PLK1, and induce G2/M arrest and apoptosis.

3.3 Targetability and anti-T-ALL performance of iNAHI *in vivo*

To study the targetability and anti-T-ALL efficacy of iNAHI *in vivo*, we employed an orthotopic T-ALL model established by tail-vein injection of CCRF-CEM cells into B-NDG mice. The successful establishment and leukemic engraftment of the orthotopic CCRF-CEM T-ALL model were verified in our previous report [45]. Following intravenous injection, iNA-Cy5 was quickly enriched in the limbs, the predominant leukemia site in mice. At 1 h postinjection, both the hindlimbs and forelimbs presented obvious Cy5 fluorescence signals, which were markedly greater than those of NA-Cy5 and were also mostly retained even after 8 h (Figure 4(a)). *Ex vivo* imaging at 8 h postinjection further corroborated the increased localization of iNA-Cy5 in the hindlimbs compared with that of NA-Cy5 (Figure 4(b)).

On day 5 after model establishment, treatment was initiated by tail vein injection of the indicated volasertib formulations with a 4-day interval for a total of five doses at 9 mg volasertib equiv./kg (Figure 4(c)). Treatment with iNAHI potently repressed the growth of T-ALL cells in peripheral blood, harboring a leukemia load of less than 0.07% on day 27 postinoculation, which was more than 480-fold lower than that of PBS-treated mice (33.9%, $p < 0.001$) (Figure 4(d) and (e)). T-ALL cells remained undetectable (< 0.06%) in iNAHI-treated mice even on day 36. In contrast, NAHI treatment only slightly decreased the leukemia load in the blood on day 27, which sharply increased to 40.6% on day 36 and led to cell death. Correspondingly, iNAHI treatment had the most pronounced survival benefit, extending the median survival of the mice to 62 days, superior to that in the PBS (32 days) and NAHI (38 days) groups ($p < 0.01$) (Figure 4(f)). Notably, T-ALL-bearing mice treated with iNAHI achieved a significant survival advantage compared with those treated with CD7-targeted strategies, including CD7-targeted CAR-T-cell therapy and polymersomal chemotherapeutics [45–47]. Moreover, the weight of the mice increased steadily after treatment with different volasertib nanoinhibitors (Figure 4(g)).

T-ALL patients are marked by abnormal expansion of leukemia cells in the bone marrow and peripheral blood, accompanied by extramedullary infiltration of the liver and spleen that results in hepatosplenomegaly [48,49]. Therefore, the T-ALL burden in mice following treatment with NAHI or iNAHI was analyzed on day 34 and compared with that in PBS-treated mice. In PBS-treated mice, T-ALL cells severely infiltrated the liver, spleen, bone marrow, lungs, and peripheral blood, with leukemic burdens reaching 81.1%, 76.0%, 83.9%, 48.7%, and 39.3%, respectively (Figure 5(a) and (b)), indicating a highly aggressive nature. Treatment with CD38-targeted iNAHI markedly inhibited T-ALL proliferation and infiltration in mice, with a percentage of T-ALL cells less than 0.1% in the bone marrow, blood and liver. This finding contrasts sharply with that of the NAHI group, in which treatment induced only a marginal reduction in the T-ALL load in the lungs and blood but left all other tissues with comparable T-ALL burdens to those of the PBS group. Consequently, iNAHI treatment effectively alleviated splenomegaly, with a normal spleen weight (~38.3 mg) comparable to that of healthy mice (Figure 5(c)). However, the mice in the PBS and NAHI groups presented severe splenomegaly, with spleen weights of 409 and 328 mg, respectively, which were 8.5–10.7-fold higher than those in the iNAHI group.

H&E staining further demonstrated the safety and superior anti-T-ALL effects of iNAHI treatment, as the hindlimbs and major organs of the mice exhibited normal histomorphology with no obvious T-ALL cells (Figure 5(d) and Figure S5). However, mice treated with PBS or NAHI presented substantial involvement of leukemia cells in the hindlimbs, liver, spleen, and lungs. Additionally, iNAHI treatment efficiently relieved hematopoietic dysfunction, a typical sign in T-ALL patients resulting from leukemia proliferation in the bone marrow [50], and resulted in substantial enrichment of hematopoietic cells within the marrow cavity (Figure 5(d)). Abnormal expansion of T-ALL cells in the bone marrow also drives the characteristic leukocytosis and thrombocytopenia observed in patients with T-ALL [51,52]. Routine blood analysis revealed that the mice in the PBS and NAHI groups presented significantly elevated white blood cell (WBC) counts and reduced platelet numbers in the blood (Figure 5(e)). This effect was effectively inhibited after treatment with iNAHI, with WBC and platelet counts similar to those in healthy controls. Collectively, these findings indicate that iNAHI enables the selective delivery of the PLK1 inhibitor volasertib to T-ALL cells, thus effectively inhibiting leukemia progression and extramedullary invasion in mice, leading to significant survival benefits with negligible side effects.

The development of targeted therapies for T-ALL faces

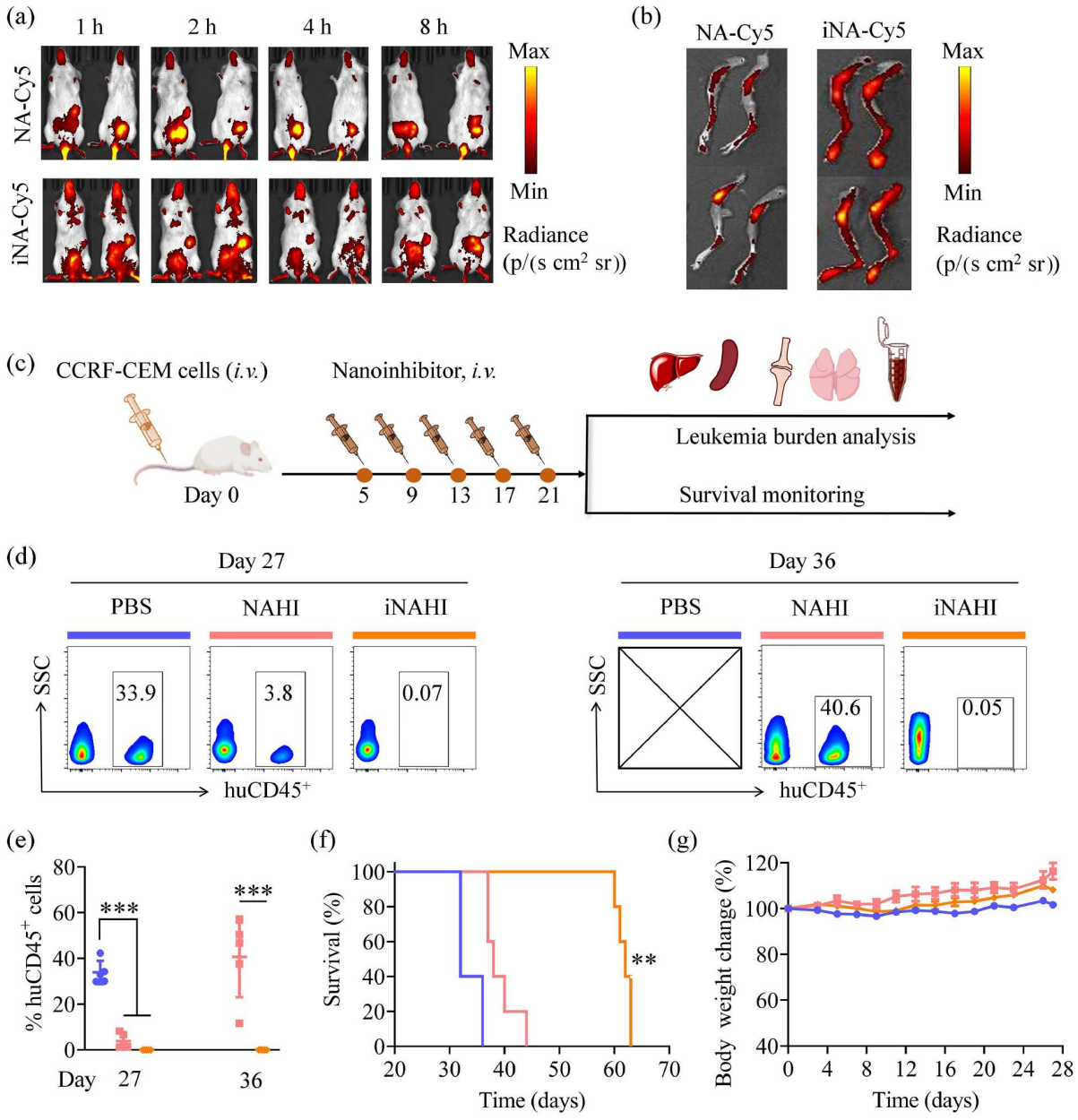

Figure 4 Biodistribution and therapeutic performance of iNAHI in orthotopic CCRF-CEM T-ALL-bearing mice. (a) *In vivo* fluorescence imaging of mice at various time points following tail vein injection with iNA-Cy5 or NA-Cy5 and (b) *ex vivo* fluorescence imaging of hindlimbs at 8 h postinjection. (c) Therapeutic and monitoring schedules. (d) Flow cytometric plots and (e) numerical quantification of leukemia burden in the circulation of mice on days 27 and 36 after treatment with PBS, NAHI or iNAHI ($n = 5$, $^{***}p < 0.001$). (f) Survival curves (iNAHI versus other controls: $^{**}p < 0.01$) and (g) body weight changes in the mice following different treatments ($n = 5$).

several critical issues as a result of the overlap of surface antigens between T-ALL blasts and normal T cells. For example, CD7-targeted CAR-T cells, as the most intensively explored targeted therapy for T-ALL, are often perplexed with fratricide and the risk of prolonged T-cell aplasia [53]. CD7-directed antibody-drug conjugates that deliver cytotoxic warheads such as monomethyl auristatin E at a low drug-to-antibody ratio of ~2.6 inevitably deplete normal T cells [54]. In contrast, CD38-targeted iNAHI with a high inhibitor-to-antibody ratio uniquely combines cost savings with improved safety and anti-T-ALL efficacy by selectively delivering the molecularly targeted agent volasertib at a markedly lower antibody dosage. Nevertheless, iNAHI monotherapy fails to eradicate all T-ALL cells and cure the mouse model. Combining it with immunotherapy, for example, immunoactive polymers [55,56], immunogenic cell death inducers [57,58], or immune metabolism modulators [59], would further amplify the anti-T-ALL efficacy.

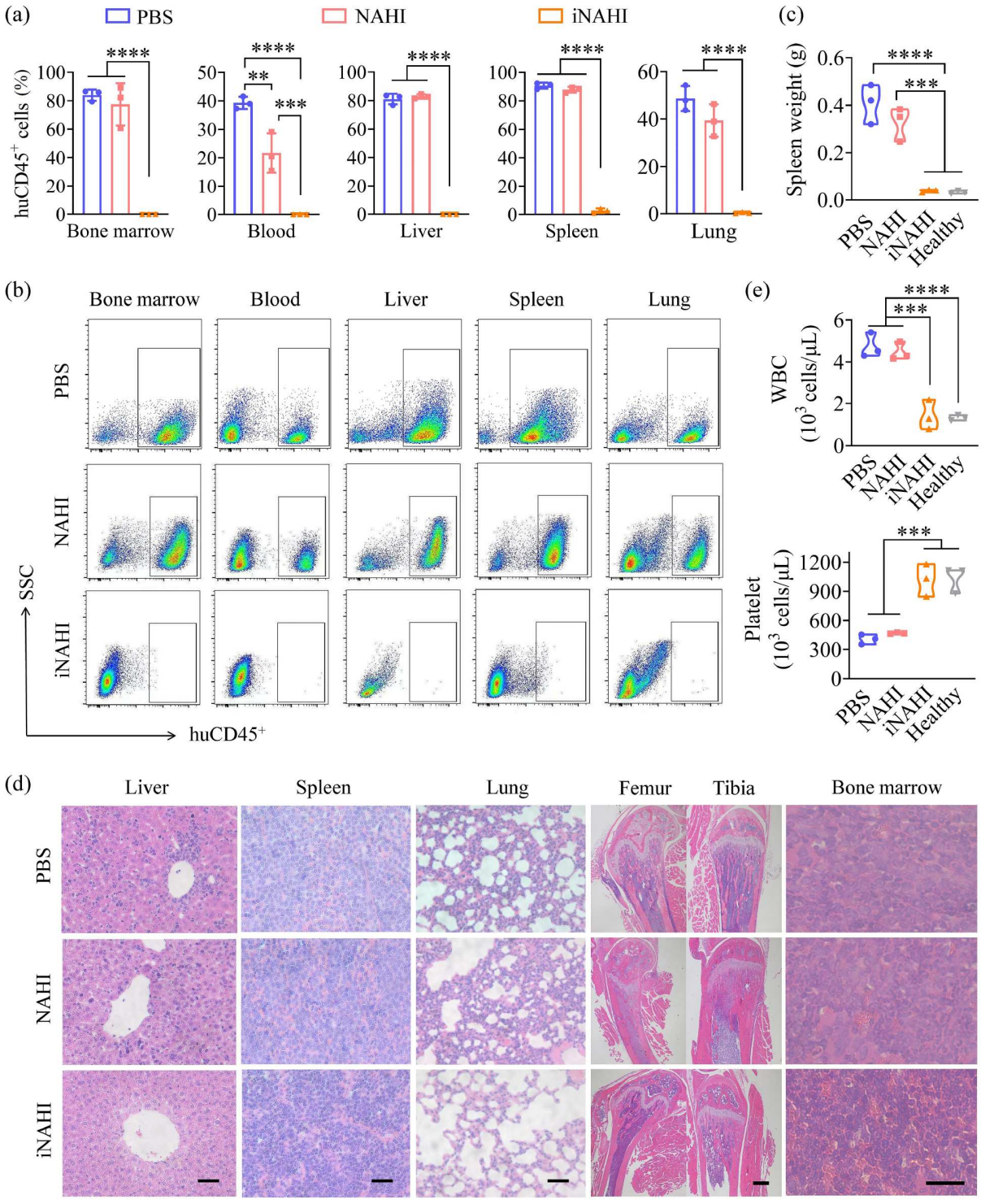

Figure 5 Leukemia burden and histological and routine blood analysis of CCRF-CEM T-ALL-bearing mice treated with different formulations (n = 3). (a) Quantitative analysis and (b) representative flow cytometric plots of the T-ALL load in the bone marrow, peripheral blood, liver, spleen, and lungs. (c) Spleen weights of the mice in different groups. (d) H&E-stained images of liver, spleen, and lung, femur and tibia harvested from different groups. Scale bars: 50 μm for liver, spleen, lung and bone marrow; 400 μm for femur and tibia. (e) WBC and platelet counts in the blood of mice. $^{**}p < 0.01$, $^{***}p < 0.001$, and $^{****}p < 0.0001$.

4 Conclusion

In this study, we reported an immuno-nanoinhibitor (iNAHI) to potentiate molecular targeted therapy for T-ALL via CD38-selective delivery of the PLK1 inhibitor volasertib. The iNAHI with daratumumab antibodies on the surface and

a high inhibitor-to-antibody ratio effectively targeted T-ALL cells, thus downregulating PLK1 and triggering apoptosis, but was safe for normal T cells. Moreover, iNAHI was able to enhance bone marrow accumulation and potently suppress leukemia expansion and extramedullary invasion in an orthotopic T-ALL mouse model, resulting in markedly improved survival benefits and normal hematopoietic function. This immuno-nanoinhibitor represents a promising precision therapeutic modality for T-ALL.

Acknowledgements This work was supported by the National Natural Science Foundation of China (Grant Nos. 52273251, 52473264) and the National Talent Supporting Program (Grant No. ZXP2025062). The schemes in the figures were created with BioRender.com.

Supporting Information The supporting information is available online at tech.scichina.com and link.springer.com. The supporting materials are published as submitted, without typesetting or editing. The responsibility for scientific accuracy and content remains entirely with the authors.

References

1 Fuentes P, García-Peydró M, Alcain J, et al. Pre-TCR-targeted immunotherapy for T cell acute lymphoblastic leukemia. Nat Immunol, 2025, 26: 1712–1725
2 Belver L, Ferrando A. The genetics and mechanisms of T cell acute lymphoblastic leukaemia. Nat Rev Cancer, 2016, 16: 494–507
3 Xu X, Zhang W, Xuan L, et al. PD-1 signalling defines and protects leukaemic stem cells from T cell receptor-induced cell death in T cell acute lymphoblastic leukaemia. Nat Cell Biol, 2023, 25: 170–182
4 Buckley M, Yeung D T, White D L, et al. T-cell acute lymphoblastic leukaemia: Subtype prevalence, clinical outcome, and emerging targeted treatments. Leukemia, 2025, 39: 1294–1310
5 Malard F, Mohty M. Acute lymphoblastic leukaemia. Lancet, 2020, 395: 1146–1162
6 Caracciolo D, Mancuso A, Polerà N, et al. The emerging scenario of immunotherapy for T-cell acute lymphoblastic leukemia: Advances, challenges and future perspectives. Exp Hematol Oncol, 2023, 12: 5
7 Pölönen P, Di Giacomo D, Seffernick A E, et al. The genomic basis of childhood T-lineage acute lymphoblastic leukaemia. Nature, 2024, 632: 1082–1091
8 Amaral P, Christie R, Gresham D O F, et al. Underlying biology, challenges and emergent concepts in the treatment of relapsed and refractory pediatric T-cell acute lymphoblastic leukemia. Leukemia, 2025, 39: 2575–2589
9 Saygin C, Giordano G, Shimamoto K, et al. Dual targeting of apoptotic and signaling pathways in T-lineage acute lymphoblastic leukemia. Clin Cancer Res, 2023, 29: 3151–3161
10 Hormann F M, Rudd S G. Nelarabine in T-cell acute lymphoblastic leukemia: Intracellular metabolism and molecular mode-of-action. Leukemia, 2025, 39: 531–542
11 Shimony S, DeAngelo D J, Luskin M R. Nelarabine: When and how to use in the treatment of T-cell acute lymphoblastic leukemia. Blood Adv, 2024, 8: 23–36
12 Jabbour E, Short N J, Jain N, et al. The evolution of acute lymphoblastic leukemia research and therapy at MD Anderson over four decades. J Hematol Oncol, 2023, 16: 22
13 Xu J, Zhu H H. Targeted treatment of T-cell acute lymphoblastic leukemia: Latest updates from the 2022 ASH Annual Meeting. Exp Hematol Oncol, 2023, 12: 30
14 Tarantino P, Ricciuti B, Pradhan S M, et al. Optimizing the safety of antibody-drug conjugates for patients with solid tumours. Nat Rev Clin Oncol, 2023, 20: 558–576
15 Weiner G J. Building better monoclonal antibody-based therapeutics. Nat Rev Cancer, 2015, 15: 361–370
16 Cappell K M, Kochenderfer J N. Long-term outcomes following CAR T cell therapy: What we know so far. Nat Rev Clin Oncol, 2023, 20: 359–371
17 Zhou S, Xu C, Wang J. *In vivo* CAR-T cell therapy and its technologies: A perspective. Sci China Technol Sci, 2025, 68: 2200209
18 Zhao L, Chang F, Tong Y, et al. A multifunctional bimetallic nanoplatform for synergic local hyperthermia and chemotherapy targeting HER2-positive breast cancer. Adv Sci, 2024, 11: 2308316
19 Tirado N, Fidyt K, Mansilla M J, et al. CAR-T cells targeting CCR9 and CD1a for the treatment of T cell acute lymphoblastic leukemia. J Hematol Oncol, 2025, 18: 69
20 Zheng H, Zhao H, Han S, et al. Chimeric antigen receptor-T cell therapy for T cell-derived hematological malignancies. Exp Hematol Oncol, 2024, 13: 117
21 Müller K, Vogiatzi F, Winterberg D, et al. Combining daratumumab with CD47 blockade prolongs survival in preclinical models of pediatric T-ALL. Blood, 2022, 140: 45–57
22 Glisovic-Aplenc T, Diorio C, Chukinas J A, et al. CD38 as a pan-hematologic target for chimeric antigen receptor T cells. Blood Adv, 2023, 7: 4418–4430
23 Koslowski S, Glauben R, Habringer S, et al. Frequent, high density expression of surface CD38 as a potential therapeutic target in adult T-lineage acute lymphoblastic leukemia. Haematologica, 2024, 109: 661–665
24 Bhatla T, Hogan L E, Teachey D T, et al. Daratumumab in pediatric relapsed/refractory acute lymphoblastic leukemia or lymphoblastic lymphoma: The DELPHINUS study. Blood, 2024, 144: 2237–2247
25 Senapati J, Jabbour E. Dar-ting at CD38 in T-cell leukemias. Blood, 2024, 144: 2162–2164
26 Brivio E, Bautista F, Zwaan C M. Naked antibodies and antibody-drug conjugates: Targeted therapy for childhood acute lymphoblastic leukemia. Haematologica, 2024, 109: 1700–1712
27 van de Donk N W C J, Richardson P G, Malavasi F. CD38 antibodies in multiple myeloma: Back to the future. Blood, 2018, 131: 13–29
28 Morandi F, Horenstein A L, Costa F, et al. CD38: A target for immunotherapeutic approaches in multiple myeloma. Front Immunol, 2018, 9: 2722
29 Shah K, Nasimian A, Ahmed M, et al. PLK1 as a cooperating partner for BCL2-mediated antiapoptotic program in leukemia. Blood Cancer J, 2023, 13: 139
30 Wang W, Zhao R, Wang Y, et al. PLK1 in cancer therapy: A comprehensive review of immunomodulatory mechanisms and therapeutic opportunities. Front Immunol, 2025, 16: 1602752
31 Van den Bossche J, Lardon F, Deschoolmeester V, et al. Spotlight on volasertib: Preclinical and clinical evaluation of a promising Plk1 inhibitor. Med Res Rev, 2016, 36: 749–786
32 Zhou C, Xia Y, Wei Y, et al. GE11 peptide-installed chimaeric polymersomes tailor-made for high-efficiency EGFR-targeted protein therapy of orthotopic hepatocellular carcinoma. Acta Biomater, 2020, 113: 512–521
33 Yu N, Zhang Y, Li J, et al. Daratumumab immunopolymersome-enabled safe and CD38-targeted chemotherapy and depletion of multiple myeloma. Adv Mater, 2021, 33: 2007787
34 Yue S, An J, Zhang Y, et al. Exogenous antigen upregulation empowers antibody targeted nanochemotherapy of leukemia. Adv Mater, 2023, 35: 2209984
35 Zhang Y, An J, Shao Y, et al. CD38-directed vincristine nanotherapy for acute lymphoblastic leukemia. Biomacromolecules, 2022, 23: 377–387
36 Tembhare P R, Sriram H, Khanka T, et al. Flow cytometric evaluation of CD38 expression levels in the newly diagnosed T-cell acute lymphoblastic leukemia and the effect of chemotherapy on its expression in measurable residual disease, refractory disease and relapsed disease: An implication for anti-CD38 immunotherapy. J Immunother Cancer, 2020, 8: e000630
37 Nieto-Jimenez C, Galan-Moya E M, Corrales-Sanchez V, et al. In-

hibition of the mitotic kinase PLK1 overcomes therapeutic resistance to BET inhibitors in triple negative breast cancer. Cancer Lett, 2020, 491: 50–59
38 Deng Q, Yue S, You F, et al. Vincristine/volasertib polymersome injection enables high-efficiency synergistic treatment of acute lymphoblastic leukemia. Acta Biomater, 2025, 200: 641–652
39 Chapagai D, Ramamoorthy G, Varghese J, et al. Nonpeptidic, polo-box domain-targeted inhibitors of PLK1 block kinase activity, induce its degradation and target-resistant cells. J Med Chem, 2021, 64: 9916–9925
40 Dimri M, Cho J H, Kang M, et al. PLK1 inhibition down-regulates polycomb group protein BMI1 via modulation of the miR-200c/141 cluster. J Biol Chem, 2015, 290: 3033–3044
41 Poyil P K, Siraj A K, Padmaja D, et al. PLK1 and FoxM1 expressions positively correlate in papillary thyroid carcinoma and their combined inhibition results in synergistic anti-tumor effects. Mol Oncol, 2024, 18: 691–706
42 Bassermann F, Frescas D, Guardavaccaro D, et al. The Cdc14B-Cdh1-Plk1 axis controls the G2 DNA-damage-response checkpoint. Cell, 2008, 134: 256–267
43 Asadi M, Taghizadeh S, Kaviani E, et al. Caspase-3: Structure, function, and biotechnological aspects. Biotech App Biochem, 2022, 69: 1633–1645
44 Ai Y, Meng Y, Yan B, et al. The biochemical pathways of apoptotic, necroptotic, pyroptotic, and ferroptotic cell death. Mol Cell, 2024, 84: 170–179
45 Zhai Z, Zhang Y, Yue S, et al. CD7-specific polymersomal vincristine delivery potentiates chemotherapy in T-cell acute lymphoblastic leukemia. Polym Sci Tech, 2026, 2: 40–47
46 Zhang T, Wang T, You F, et al. Nanobody-based anti-CD22-chimeric antigen receptor T cell immunotherapy exhibits improved remission against B-cell acute lymphoblastic leukemia. Transplant Immunol, 2022, 71: 101538
47 Dong Y, You F, Zhang Y, et al. CD7 nanobody-based immunonanotoxin for targeted treatment of T-cell acute lymphoblastic leukemia. ACS Appl Nano Mater, 2024, 7: 7195–7202
48 Buonamici S, Trimarchi T, Ruocco M G, et al. CCR7 signalling as an essential regulator of CNS infiltration in T-cell leukaemia. Nature, 2009, 459: 1000–1004
49 Yang F, Feng W, Wang H, et al. Monocyte-derived leukemia-associated macrophages facilitate extramedullary distribution of T-cell acute lymphoblastic leukemia cells. Cancer Res, 2020, 80: 3677–3691
50 Álvarez-Zúñiga C D, Garza-Veloz I, Martínez-Rendón J, et al. Circulating biomarkers associated with the diagnosis and prognosis of B-cell progenitor acute lymphoblastic leukemia. Cancers, 2023, 15: 4186
51 Zhang Z, Yang K, Zhang H. Targeting leukemia-initiating cells and leukemic niches: The next therapy station for T-cell acute lymphoblastic leukemia? Cancers, 2022, 14: 5655
52 Hunger S P, Mullighan C G. Acute lymphoblastic leukemia in children. N Engl J Med, 2015, 373: 1541–1552
53 Oh B L Z, Vinanica N, Wong D M H, et al. Chimeric antigen receptor T-cell therapy for T-cell acute lymphoblastic leukemia. Haematologica, 2024, 109: 1677–1688
54 Zhang J, Jain A, Milhas S, et al. An antibody-drug conjugate with intracellular drug release properties showing specific cytotoxicity against CD7-positive cells. Leukemia Res, 2021, 108: 106626
55 Wei Q, Xin H, Wang X, et al. Unimolecular chiral poly(amino acid)s as adjuvants of nanovaccines for augmented cancer immunotherapy. Chin Chem Lett, 2025, 36: 111477
56 Wang H, Li H, Wang X, et al. Immunologically effective chiral polymers to potentiate anti-cancer immune responses. Polym Sci Tech, 2025, 1: 809–811
57 Wang Y, Li H, Lin J, et al. Engineering nanozyme immunomodulator with magnetic targeting effect for cascade-enzyodynamic and ultrasound-reinforced metallo-immunotherapy in prostate carcinoma. Nat Commun, 2025, 16: 1876
58 Zhao L, Tong Y, Yin J, et al. Photo-activated oxidative stress amplifier: A strategy for targeting glutathione metabolism and enhancing ROS-mediated therapy in triple-negative breast cancer treatment. Small, 2024, 20: 2403861
59 Qin C, Yang G, Wei Q, et al. Multidimensional role of amino acid metabolism in immune regulation: From molecular mechanisms to therapeutic strategies. Chem Res Chin Univ, 2025, 41: 1–14